PHYSICAL REVIEW MATERIALS **3**, 013609 (2019)

First-principles study on the grain boundary embrittlement of bcc-Fe by Mn segregation

Kazuma Ito,[1,2,*] Hideaki Sawada,[2] and Shigenobu Ogata[1,3,†]
[1] *Graduate School of Engineering Science, Osaka University, 1-3 Machikaneyama, Toyonaka, Osaka 560-8531, Japan*
[2] *Advanced Technology Research Laboratories, Nippon Steel & Sumitomo Metal Corporation,*
1-8 Fuso-Cho, Amagasaki, Hyogo 660-0891, Japan
[3] *Elements Strategy Initiative for Structural Materials (ESISM), Kyoto University, Kyoto, Kyoto 606-8501, Japan*

(Received 28 September 2018; published 31 January 2019)

Developing steels with high strength and ductility is needed in order to improve the mechanical reliability and environmental performance of engineering products. The addition of Mn is a key technology for developing next-generation high-strength steels. However, the addition of Mn leads to a serious side effect, grain boundary (GB) embrittlement, which decreases the mechanical toughness of steels. Understanding the mechanism of GB embrittlement due to Mn is an essential process for improving the toughness of steels containing Mn. In this work, in order to reveal the fundamental mechanism of GB embrittlement by Mn, the effect of Mn on the cleavage fracture of bcc-Fe GBs, especially the influence of the difference in the magnetic coupling state between Mn and Fe, is investigated using uniaxial tensile simulations of the bcc-Fe $\Sigma3(111)$ GB with and without Mn segregation using the first-principles density functional theory (DFT). The uniaxial tensile simulations demonstrate that Mn decreases the cleavage-fracture energy of the GB. In particular, the ferromagnetically coupled Mn substantially decreases the cleavage-fracture energy of the GB, promoting cleavage fracture. When ferromagnetically coupled Mn is present in the bcc-Fe GBs, the electrons contributing to the bonds between Mn and the surrounding Fe atoms easily localize to the Mn atom with increasing stress, and the bonding between Mn and the surrounding Fe atoms rapidly weakens, leading to a cleavage fracture of the GBs at a lower stress and strain. This unusual behavior is derived from the stability of the nonbonding Mn as a result of its half-filled d shell. These results show that the local magnetic state in GBs is one of the factors determining the macroscopic mechanical properties of steels containing Mn.

DOI: 10.1103/PhysRevMaterials.3.013609

I. INTRODUCTION

Steel is widely used as a structural material and remains one of the most important materials. Mn is a major alloying element in steel and has been widely added to induce solid-solution strengthening at room temperature and to increase hardenability. In recent years, a so-called third-generation advanced high-strength steel has been developed to reduce the environmental burden and improve safety. As a promising candidate third-generation advanced high-strength steel, high-strength steel containing a large amount of Mn has been extensively studied, and the utilization of Mn is currently expanding [1–15]. Therefore, understanding the effects of Mn addition to steel materials is important.

Mn is known to contribute to the strengthening of steels while adversely affecting toughness because of grain-boundary (GB) embrittlement. Yamanaka *et al.* showed that the ductile brittle transition temperature (DBTT) of low-carbon steel decreases with increasing Mn concentration, reaching a minimum at 2 wt.% Mn and then increasing with higher Mn concentrations [16]. Tanaka *et al.* examined the effect of Mn addition on the DBTT and the activation energy for dislocation glide in experiments using ultralow-carbon steels, and they showed that although Mn increases the dislocation mobility at low temperatures, both the DBTT and the fraction of intergranular fracture surface (FS) increase with increasing Mn concentration [17]. They explained these results on the basis of the decreased cleavage-fracture energy of bcc-Fe GBs with increasing Mn concentration.

As described, Mn is a GB embrittlement element in steels. Therefore, deterioration of toughness due to GB embrittlement in steels containing a large amount of Mn is a concern. In particular, as the strength of the material increases, its susceptibility to GB embrittlement also increases [18]. Such GB embrittlement by Mn may pose a serious problem in the future, and the fundamental mechanism of GB embrittlement by Mn has not been clarified.

In this study, in order to clarify the fundamental mechanism of the GB embrittlement by Mn from the viewpoint of the electron theory of metals, we use the first-principles density functional theory (DFT) to investigate the effect of Mn on the cleavage fracture of bcc-Fe GBs by performing uniaxial tensile simulations on the bcc-Fe $\Sigma3(111)$ GB with and without Mn segregation. Mn in bcc-Fe is well known to have two magnetic coupling states: an antiferromagnetic (AFM) Mn-Fe magnetic coupling state and a ferromagnetic (FM) Mn-Fe magnetic coupling state. The difference in energy between these two magnetic coupling states is small. In addition, the magnetic coupling state can change depending on the concentration of Mn [19–22] or the presence of C [23].

---

[*] Corresponding author: ito.nn3.kazuma@jp.nssmc.com
[†] Corresponding author: ogata@me.es.osaka-u.ac.jp

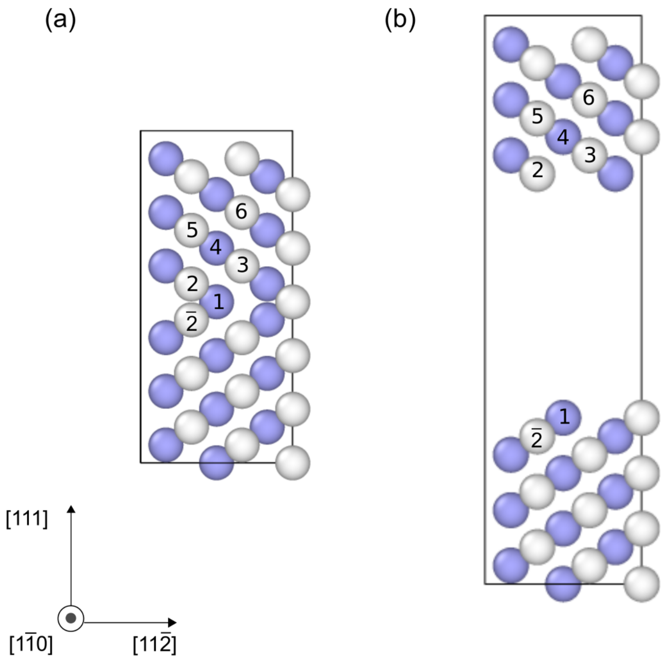

FIG. 1. Model and notation for (a) bcc-Fe $\Sigma3(111)/[1\bar{1}0]$ GB and (b) FS of bcc-Fe (111). The blue and white circles indicate Fe atoms on $(1\bar{1}0)$ and $(2\bar{2}0)$, respectively.

Therefore, we investigated the effect of the magnetic coupling state of Mn on the cleavage fracture of GBs by conducting simulations for both magnetic coupling states.

II. COMPUTATIONAL METHODS

Calculations were performed on GB models that included the bcc-Fe $\Sigma3(111)/[1\bar{1}0]$ GBs shown in Fig. 1(a). Most grain boundaries in polycrystalline bcc-Fe are random GBs. However, these GBs are difficult to model by DFT because of the high computational cost. A study using the classical molecular dynamics method showed that the GB energy of the $\Sigma3(111)/[1\bar{1}0]$ GB is similar to that of random GBs [24]. Furthermore, by calculating the effects of a segregated element on the cleavage-fracture energy or cleavage-fracture stress of the $\Sigma3(111)/[1\bar{1}0]$ GB by the uniaxial tensile simulations using DFT, researchers have well reproduced the corresponding experimental results related to GB embrittlement or strengthening [25–27].

The size of the GB model used in the present work was $4.01\times6.95\times15.2$ Å^3. The GB model contained 36 atoms and included two $\Sigma3(111)/[1\bar{1}0]$ GBs owing to the periodic boundary conditions. The spin-polarized electronic structure calculations and structural optimization for the uniaxial tensile simulations and calculation of segregation energies explained later were performed using the Vienna *ab initio* simulation package with the projector-augmented wave potentials [28,29]. The exchange-correlation effects were treated in the framework of the generalized gradient approximation (GGA) using the Perdew-Burke-Ernzerhof parametrization [30]. The cutoff energy for the plane-wave basis set was 520 eV. The Monkhorst-Pack k-point mesh [31] was $6\times4\times2$. The Methfessel-Paxton smearing method [32] with a 0.2 eV width was used.

In the uniaxial tensile simulations, structural optimization, including the cell shape, was performed first. An incremental engineering strain of uniaxial tension in the [111] direction, which is normal to the GB plane, was then applied to the cell as 2% of the relaxed cell shape, and the atomic positions were fully relaxed. The cell lengths in the $[1\bar{1}0]$ and $[11\bar{2}]$ directions were fixed in order to reduce the computational cost, which means Poisson's ratio was neglected. This step was iterated until cleavage fracture occurred. At each step, all of the atoms were relaxed according to the Hellman-Feynman forces until all of the forces acting on each atom were less than 0.02 eV/Å. The uniaxial tensile stress in the direction perpendicular to the GB plane was obtained by dividing the change in energy by the change in volume at each step. In the uniaxial tensile simulation, the stress increased as the tensile strain increased, and then an abrupt stress reduction occurred at a certain strain. This phenomenon is hereinafter referred to as GB cleavage fracture. The cleavage-fracture energy was calculated as the difference between the maximum energy until GB cleavage fracture and the energy before the tensile strain was applied. The cleavage-fracture stress was calculated as the maximum stress until GB cleavage fracture.

The validity of the calculation conditions was confirmed as follows. We confirmed that the cleavage-fracture energies converged within the range of 10 meV by comparing the calculation results between 270 eV and 520 eV for the cutoff energy and comparing the calculation results between $6\times4\times2$ and $12\times8\times4$ for the k-point mesh. We also confirmed that the energy at the same tensile strain converged within the range of 10 meV even when the step width of the engineering strain was changed from 2% to 1%. The critical tensile strain at which GB cleavage fracture occurred also converged within ±1%.

In the models of Mn-segregated GBs, the Mn atom was placed at Site 1 indicated in Fig. 1(a). In order to determine the most favorable segregation site of Mn, we calculated the segregation energies of Mn for two magnetic coupling states. The segregation energies were calculated from the difference between the energy change when Fe at Site 5 (in the bulk) was replaced with Mn and the energy change when Fe at Sites 1–4 (in the GB) was replaced with Mn. In the bulk site, the energy difference between the two magnetic coupling states was 0.04 eV, and the energy in the AFM Mn-Fe magnetic coupling state was slightly lower. In both magnetic coupling states, Site 1 was the most favorable segregation site, and the segregation energies in the AFM and FM Mn-Fe magnetic coupling state were 0.49 eV and 0.06 eV, respectively [33]. In order to investigate the influence of the magnetic coupling states of Mn on the GB cleavage fracture, we performed uniaxial tensile simulations for three cases: (1) GB without Mn segregation (clean GB), (2) GB with FM-coupled Mn at Site 1 (FM Mn-segregated GB), and (3) GB with AFM-coupled Mn at Site 1 (AFM Mn-segregated GB).

In order to investigate the role of tensile stress in the GB embrittlement by Mn, we evaluated the influence of Mn at Site 1 on the GB cleavage fracture for the two magnetic coupling states within the Rice-Wang model. In the Rice-Wang model, we evaluated the influence of segregation elements on GB

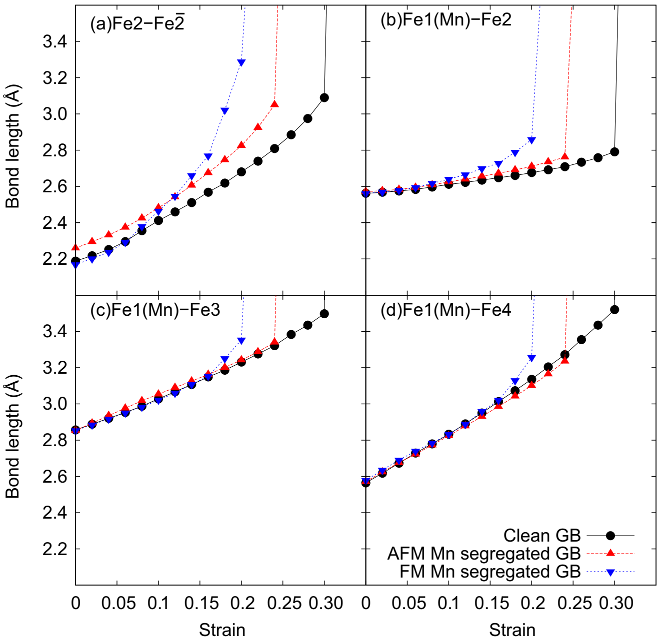

FIG. 2. Variations in the bond lengths of (a) Fe2-Fe$\bar{2}$, (b) Fe1(Mn)-Fe2, (c) Fe1(Mn)-Fe3, and (d) Fe1(Mn)-Fe4 as a function of strain.

cleavage fracture by calculating the embrittlement potency $(\Delta E_{\mathrm{GB}} - \Delta E_{\mathrm{FS}})$, which is the energy difference between the segregation energy for GBs before tensile stress was applied (ΔE_{GB}) and the segregation energy for FSs after cleavage fracture (ΔE_{FS}). For calculations of segregation energy for the FSs, we used the FS model shown in Fig. 1(b). The size of the FS model was $4.01 \times 6.95 \times 25.2$ Å^3. This model contained 36 atoms and included two (111) surfaces and the $\Sigma3(111)/[1\bar{1}0]$ GB. A vacuum region with a thickness of 1 nm was provided to prevent interaction between the FSs. The segregation energies for the FSs were calculated from the difference between the energy change when Fe at Site 5 (in the bulk) was replaced with Mn and the energy change when Fe at Site 1 (in the FS) was replaced with Mn.

III. RESULTS AND DISCUSSION

Figure 2 shows the variations in bond lengths of (a) Fe2-Fe$\bar{2}$, (b) Fe1(Mn)-Fe2, (c) Fe1(Mn)-Fe3, and (d) Fe1(Mn)-Fe4 as a function of tensile strain. Atomic structures before applying tensile stress and after cleave fracture are shown in Fig. 3. In all of the GB models, the bond lengths monotonically increase with increasing tensile strain. When the tensile strain reaches a certain value, the bond lengths rapidly increase. The differences in the bond lengths of Fe2-Fe$\bar{2}$ and Fe1(Mn)-Fe2 with increasing tensile strain among the GB models appear in a lower-strain region compared with the differences in the bond lengths of Fe1(Mn)-Fe3 and Fe1(Mn)-Fe4. These results suggest that the Fe2-Fe$\bar{2}$ and Fe1(Mn)-Fe2 bonds are more strongly affected by Mn segregation. In the Mn-segregated GBs for both magnetic coupling states, rapid increases in bond lengths occur with smaller tensile strain compared with the clean GB. In particular, the change in the FM Mn-segregated GB is remarkable.

Figures 4(a) and 4(b) show the stress-strain curves and energy-strain plots obtained from the uniaxial tensile simulations, respectively. In all of the GB models, the stress increases with increasing tensile strain. After the stress reaches its maximum value, GB cleavage fracture occurs. The tensile strain immediately before the cleavage fracture is hereinafter referred to as fracture strain. The results for the clean GB agree well with the results reported in a previous study [26]. In the AFM Mn-segregated GB, the fracture strain, cleavage-fracture energy, and cleavage-fracture stress decrease compared with those in the clean GB. In particular, FM-coupled Mn significantly reduces the fracture strain, cleavage-fracture energy, and cleavage-fracture stress. This behavior corresponds to a sharp increase in the bond length with increasing tensile strain in the FM Mn-segregated GB, indicating that FM-coupled Mn at GBs remarkably promotes GB cleavage fracture. Tanaka *et al.* reported that Mn increases the DBTT of bcc-Fe despite increasing the dislocation mobility [17]. Their results suggest that Mn markedly promotes GB cleavage fracture. Our calculation results correspond well with this experimental result.

Table I lists the calculated values of segregation energy for GBs (ΔE_{GB}) and FSs (ΔE_{FS}) and the embrittlement potency

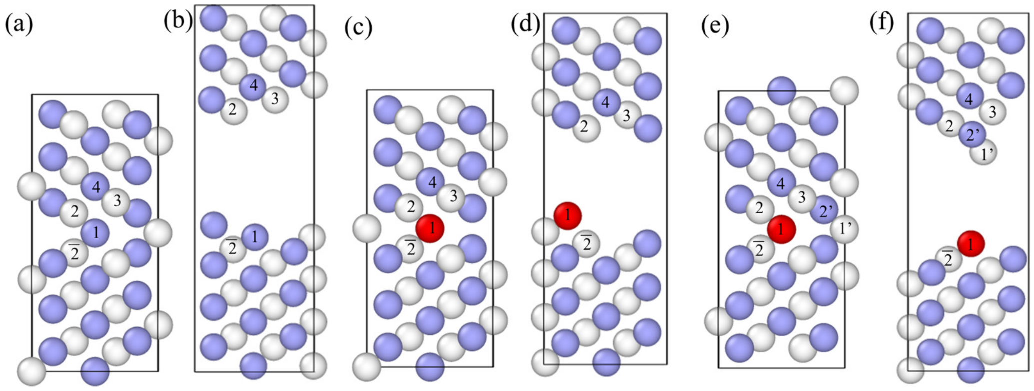

FIG. 3. Atomic structures of (a) clean GB before applying tensile stress, (b) clean GB after cleave fracture, (c) AFM Mn segregated GB before applying tensile stress, (d) AFM Mn segregated GB after cleave fracture, (e) FM Mn segregated GB before applying tensile stress, and (f) FM Mn segregated GB after cleave fracture. The blue and white circles indicate Fe atoms on $(1\bar{1}0)$ and $(2\bar{2}0)$, respectively. The red circles indicate Mn atoms.

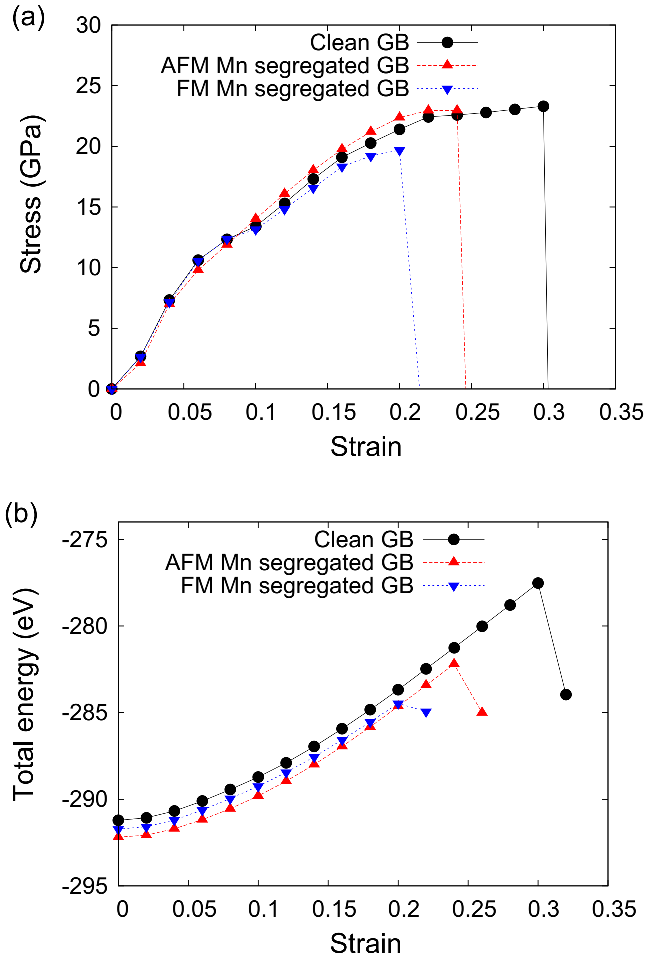

FIG. 4. (a) Stress-strain curves and (b) energy-strain plot obtained using data from the uniaxial tensile simulations for the clean GB, the AFM Mn-segregated GB, and the FM Mn-segregated GB.

($\Delta E_{\mathrm{GB}} - \Delta E_{\mathrm{FS}}$) for the two magnetic coupling states of Mn. In the Rice-Wang model, the embrittlement potency is almost zero in the AFM magnetic coupling state and 0.05 eV in the FM magnetic coupling state, indicating that the influence on the GB cleavage energy is extremely small. Quantitatively, these results do not agree with the results of the uniaxial tensile simulations. This difference between the two methods is derived from the fact that, in the Rice-Wang model, the effect of the segregated Mn on the bonding state of the atoms near the GB when stress is applied to the GB is disregarded. That is, the essence of the promotion of GB cleavage fracture by Mn lies in the influence of Mn on the change in the bonding state of atoms near the GB in response to stress applied to the GB.

TABLE I. Segregation energies of Mn at Site 1 in the GB model, ΔE_{GB}, and at Site 1 in the FS model shown in Fig. 1, ΔE_{FS}, and the embrittlement potencies, $\Delta E_{\mathrm{GB}} - \Delta E_{\mathrm{FS}}$, for two magnetic coupling states (in eV).

System	ΔE_{GB}	ΔE_{FS}	$\Delta E_{\mathrm{GB}} - \Delta E_{\mathrm{FS}}$
AFM Mn segregated GB	−0.49	−0.49	0.00
FM Mn segregated GB	−0.06	−0.11	0.05

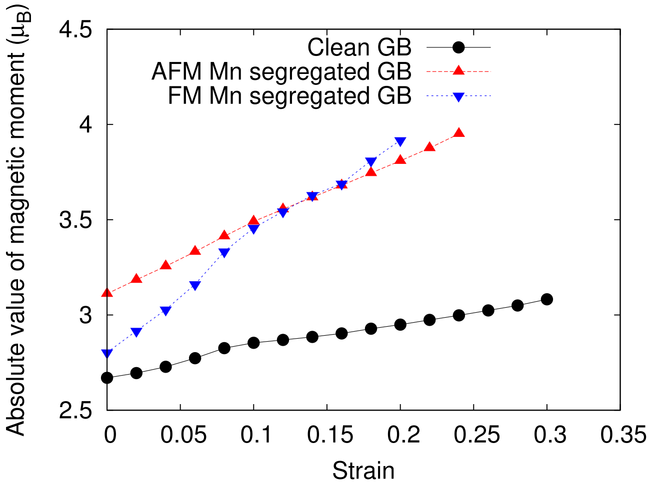

FIG. 5. Variations in the absolute values of magnetic moments of the Fe1 atom in the clean GB and Mn atoms in the Mn-segregated GBs as a function of strain.

Zhong *et al.* used the local-density approximation (LDA) to calculate the embrittlement potency of AFM-coupled Mn for the same bcc-Fe $\Sigma3(111)/[1\bar{1}0]$ GB and segregation site as in our study and showed that the embrittlement potential is 0.2 eV [34], which is inconsistent with our result. This discrepancy can be derived from the difference in the exchange-correlation function. Wachowicz *et al.* calculated the cohesive energy of the bcc-Fe $\Sigma5(210)$ GB with both GGA and LDA and showed that there is a large discrepancy in the absolute value of the cohesive energies depending on the exchange-correlation function [35]. Furthermore, they calculated embrittlement potencies of B at an interstitial site and a substitutional site of the same GB with GGA and showed that the obtained embrittlement potencies of both sites gave large differences with the result of previous study [36] using LDA. For example, in the case of the substitutional site, the embrittlement potencies of B were −0.58 eV and 0.34 eV using GGA and LDA, respectively. Based on the results of the cohesive energies, they concluded that the cause of this discrepancy is mainly due to the difference of the exchange-correlation function. Thus, the difference of the exchange-correlation function can cause the discrepancy in embrittlement potency of segregated elements.

The performance of GGA and LDA in solids is controversial. Wang *et al.* pointed out that there are substantial errors in the lattice constant and magnetic moments of Fe, as well as a prediction of the wrong ground state of nonmagnetic hcp-Fe [37]. After that, Asada *et al.* showed that GGA correctly reproduces the cohesive energy, lattice constant, magnetic moment, and ground state of Fe [38]. However, these results do not necessarily mean that GGA is more suitable than LDA to describe the bonding properties of GBs of Fe [39]. Therefore, although it is desirable to perform the calculations with both GGA and LDA, we found that the ferromagnetic bcc-Fe $\Sigma3(111)/[1\bar{1}0]$ GB is structurally and magnetically unstable when the structural optimization including the cell shape is performed using LDA. For this reason, we could not perform the uniaxial tensile simulations with LDA. On the other hand, although the embrittlement potencies of Mn

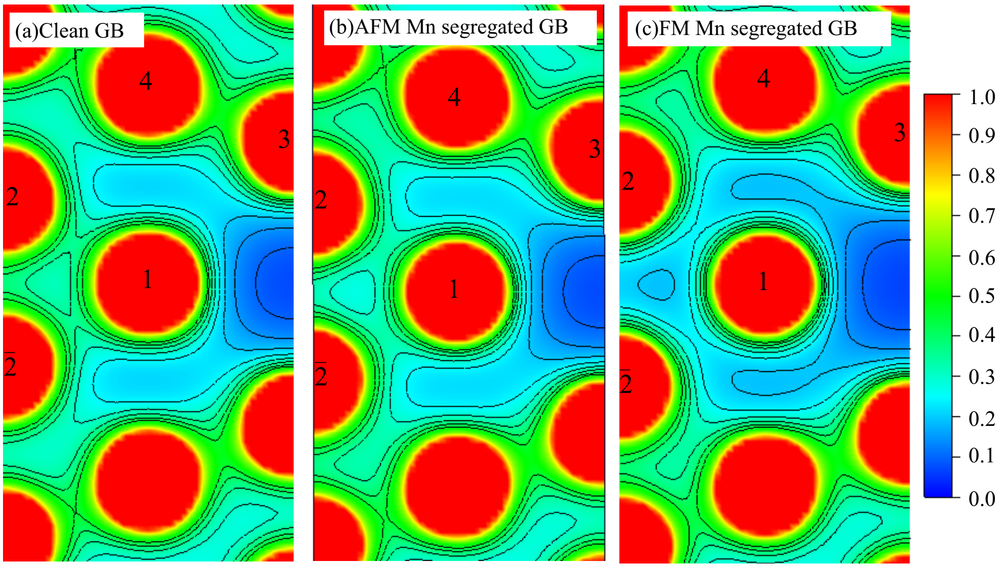

FIG. 6. Charge-density distributions in the plane crossing atoms of Fe1 (or Mn), Fe2, and Fe$\bar{2}$ (in 10^{-1} electrons/a_0^3).

are quantitatively different between the previous study using LDA and the present study using GGA, both calculations are qualitatively the same in that they cannot predict the large change of the cleavage-fracture energy by Mn segregation. For these reasons, we discuss the effect of Mn on the cleavage fracture of the GB based on the calculation results using GGA, which can reproduce the ground state of the GB of Fe even in the calculation including the structural optimization.

Figure 5 shows the variations in the absolute values of magnetic moments of the Fe1 atom in the clean GB and the Mn atoms in the Mn-segregated GBs as a function of tensile strain. In all of the GB models, the magnetic moment increases as the tensile strain increases. This increase in the magnetic moment of Mn is larger than that of Fe. This behavior of magnetic moments means that as the tensile strain increases, the orbital hybridization with the surrounding atoms weakens and the electrons localize to each atom. In particular, the magnetic moment of Mn in the FM Mn-segregated GB drastically increases with increasing tensile strain, which indicates that bonding with the surrounding Fe atoms is remarkably weakened by the tensile strain.

Figure 6 shows charge-density distributions in the vicinity of the GB at 20% tensile strain, which is the strain immediately before the cleavage fracture in the FM Mn-segregated GB. The charge-density distributions in the plane crossing atoms of Fe1 (or Mn), Fe2, and Fe$\bar{2}$, whose bonding length drastically changes, are shown. The charge density between Mn and neighboring Fe atoms is smaller in the Mn-segregated GBs than in the clean GB. In particular, the charge density between surrounding Fe atoms is much lower in the FM Mn-segregated GB than in the other GB models, indicating that Mn is hardly bonded to the surrounding Fe atoms.

Figure 7 shows the change in the minimum value of the charge density on the straight line connecting Fe1 (or Mn) and Fe2 with increasing tensile strain. Before a tensile strain was applied, almost no difference in charge density was observed among the GB models. However, compared with the clean GB, the Mn-segregated GBs exhibit a greater reduction in charge density with increasing tensile strain. In particular, in the FM Mn-segregated GB, the reduction of the charge density is remarkable. This trend corresponds to the weakening of the bonding suggested by the change in the magnetic moment with increasing tensile strain. These results suggest the relationship between the embrittlement by the FM-coupled Mn and the stability of Mn as the nonbonding state. The nonbonding state of Mn is more stable than that of other transition metals, such as Fe, because Mn atoms have a half-filled d shell. Therefore, upon application of a tensile strain, the near-Mn electrons that contribute to bonding with the surrounding Fe atoms tend to localize to the Mn atom, and the Mn easily transitions to an almost-nonbonding atom. In fact, in the FM-coupled Mn-segregated GB, the bond lengths of Mn-Fe3 and Mn-Fe4 increase drastically from the strain of 16%, indicating that all of the bonds between the Mn and the

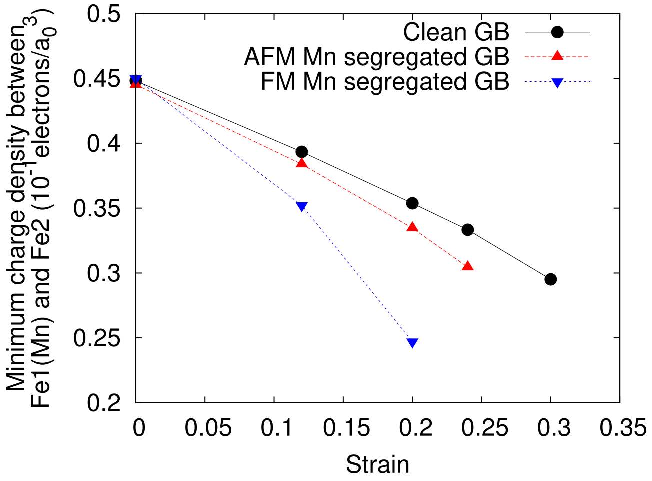

FIG. 7. Variations in the change in the minimum value of the charge density on the straight line connecting Fe1 (or Mn) and Fe2 as a function of strain.

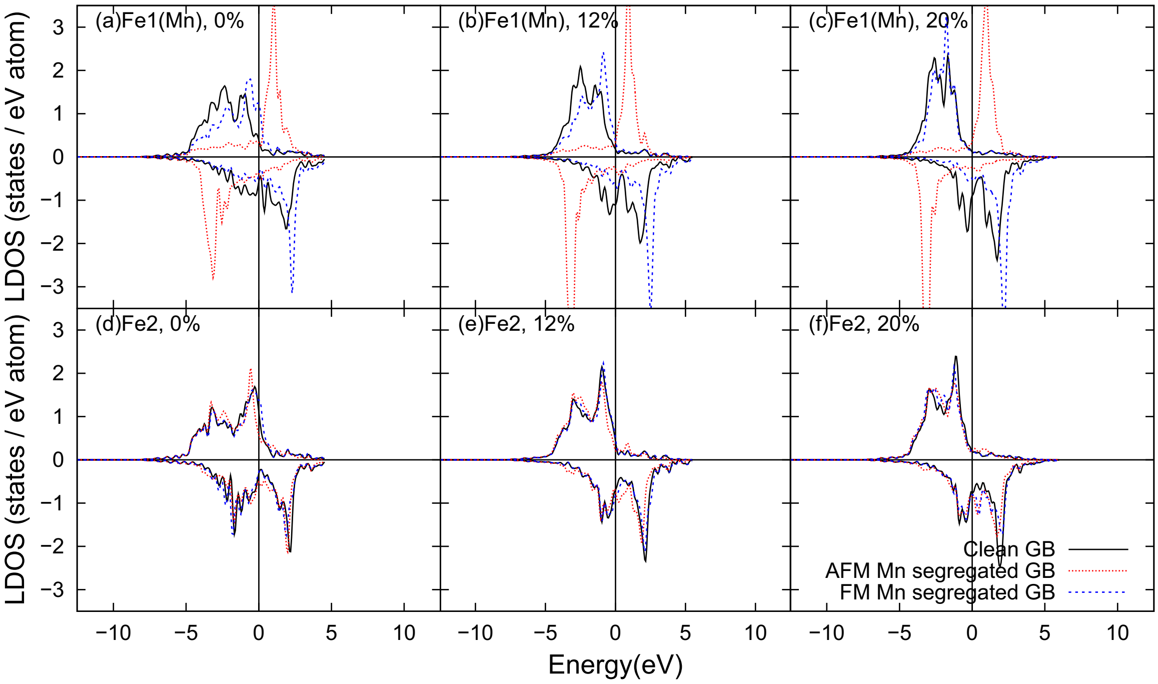

FIG. 8. LDOS for Fe1 atom in the clean GB and the Mn atoms in the Mn-segregated GBs at a strain of (a) 20%, (b) 12%, and (c) 0%. LDOS for Fe2 atom in the clean GB and the Mn-segregated GBs at a strain of (d) 0%, (e) 12%, and (f) 20%.

surrounding Fe atoms are weakened by the transition of the Mn to an almost-nonbonding Mn atom.

On the other hand, AFM-coupled Mn has a minor effect on the cleavage fracture of GBs. The local density of states (LDOS) for the Fe1 atom in the clean GB and for the Mn atoms in the Mn-segregated GBs is shown in Fig. 8. In the AFM Mn-segregated GB, the majority bands of Mn are shifted to the lower-energy side compared with those of Mn in the FM Mn-segregated GB. This shift is attributed to the strong orbital hybridization between the majority bands and the minority bands between Mn and Fe in the AFM magnetic coupling state. Therefore, the band energy of the AFM magnetic coupling state is lower than that of the FM magnetic coupling state. This reduction in the band energy indicates that the orbital hybridization between the majority band and the minority band caused by the AFM magnetic coupling can provide additional resistance to the weakening of the bonding compared with that in the FM coupling state.

Finally, we noted that GB embrittlement by FM-coupled Mn can occur in real systems. As previously described, the ground state of the GB with Mn segregation is the AFM coupling state in this study. However, the energy in the case where FM-coupled Mn exists at Site 1 is lower than that in the case where AFM-coupled Mn exists at Site 5, which corresponds to the bulk site. Furthermore, the ground state is known to change from the AFM coupling state to the FM coupling state, with an increase in Mn concentration in the bulk of bcc-Fe [19–22]. Therefore, if the concentration of Mn at the GB is increased with the increase in the amount of Mn added or the GB segregation caused by the heat treatment, FM-coupled Mn will likely exist at the GB. In addition, in the bulk of bcc-Fe, the presence of C in a site close to Mn is known to stabilize the FM coupling state, which becomes the ground state [23]. It is known that in bcc-Fe, C has an extremely high GB segregation energy [40–42] and increases the cleavage-fracture energy [25], preventing the GB fracture [41,42]. Because of the high segregation energy, even if the amount of C is 10 wt.ppm, which is the level contained as impurities of iron raw materials, C is concentrated to more than 1 at.% in the GBs [41]. In fact, all alloys used in the experiments described above contain more than 10 wt.ppm of C [16,17] and typical steel materials contain 0.02 wt.% or more C. Therefore, FM-coupled Mn is reasonably assumed to also be stabilized at GBs. In both cases, as long as the bonds between Mn and Fe at the GB dominate the cleavage fracture of the GB, the GB embrittlement by FM-coupled Mn can be caused by the aforementioned mechanism.

IV. CONCLUSION

In order to clarify the fundamental mechanism of GB embrittlement by Mn from the viewpoint of the electron theory of metals, we investigated the effect of Mn on the cleavage fracture of bcc-Fe GBs by performing uniaxial tensile simulations using the first-principles DFT for three cases: (1) a GB without Mn segregation (clean GB), (2) a GB with FM-coupled Mn, and (3) a GB with AFM-coupled Mn. The uniaxial tensile simulations show that both antiferromagnetically and ferromagnetically coupled Mn decrease the cleavage-fracture energy of the GB. In particular, ferromagnetically coupled Mn substantially decreases the cleavage-fracture energy of the GB, promoting the cleavage fracture. An analysis of the electronic structures shows that when ferromagnetically coupled Mn exists in the bcc-Fe GBs, the electrons contributing to the bonds between Mn and surrounding Fe atoms easily localize to the Mn atom with increasing stress, and the bonding between Mn and the surrounding Fe atoms rapidly weakens, causing the cleavage fracture of GBs with lower stress and strain. This unusual behavior is derived from the stability of the nonbonding Mn with a half-filled d shell. These results show that the local magnetic state in GBs is one of the factors determining the macroscopic mechanical properties of steels containing Mn.

ACKNOWLEDGMENTS

S.O. acknowledges the support by JSPS KAKENHI Grant Nos. JP18H05453, JP17H01238, and JP17K18827, and the Elements Strategy Initiative for Structural Materials (ESISM).

[1] R. L. Miller, Metall. Mater. Trans. B **3**, 905 (1972).

[2] T. Furukawa, H. Huang, and O. Matsumura, Mater. Sci. Technol. **10**, 964 (1994).

[3] D.-W. Suh, S.-J. Park, T.-H. Lee, C.-S. Oh, and S.-J. Kim, Metall. Mater. Trans. A **41**, 397 (2009).

[4] T. Hanamura, S. Torizuka, A. Sunahara, M. Imagumbai, and H. Takechi, ISIJ Int. **51**, 685 (2011).

[5] C. Wang, J. Shi, C. Y. Wang, W. J. Hui, M. Q. Wang, H. Dong, and W. Q. Cao, ISIJ Int. **51**, 651 (2011).

[6] H. F. Xu, J. Zhao, W. Q. Cao, J. Shi, C. Y. Wang, J. Li, and H. Dong, ISIJ Int. **52**, 868 (2012).

[7] D. W. Suh, J. H. Ryu, M. S. Joo, H. S. Yang, K. Lee, and H. K. D. H. Bhadeshia, Metall. Mater. Trans. A **44**, 286 (2013).

[8] C. Zhao, C. Zhang, W. Cao, Z. Yang, H. Dong, and Y. Weng, ISIJ Int. **54**, 2875 (2014).

[9] H. Xu, W. Cao, H. Dong, and J. Li, ISIJ Int. **55**, 662 (2015).

[10] P. J. Gibbs, B. C. De Cooman, D. W. Brown, B. Clausen, J. G. Schroth, M. J. Merwin, and D. K. Matlock, Mater. Sci. Eng., A **609**, 323 (2014).

[11] N. Nakada, K. Mizutani, T. Tsuchiyama, and S. Takaki, Acta Mater. **65**, 251 (2014).

[12] H. Natsumeda, A. Kitahara, and S. Hashimoto, ISIJ Int. **57**, 945 (2017).

[13] C. Shao, W. Hui, Y. Zhang, X. Zhao, and Y. Weng, Mater. Sci. Eng., A **682**, 45 (2017).

[14] B. Sun, F. Fazeli, C. Scott, B. Guo, C. Aranas, X. Chu, M. Jahazi, and S. Yue, Mater. Sci. Eng., A **729**, 496 (2018).

[15] F. Yang, H. Luo, E. Pu, S. Zhang, and H. Dong, Int. J. Plast. **103**, 188 (2018).

[16] K. Yamanaka and M. Kowaka, J. Jpn. Inst. Met. **43**, 1151 (1979).

[17] M. Tanaka, K. Matsuo, N. Yoshimura, G. Shigesato, M. Hoshino, K. Ushioda, and K. Higashida, Mater. Sci. Eng., A **682**, 370 (2017).

[18] S. Takayama, T. Ogura, S.-C. Fu, and C. J. McMahon, Metall. Trans. A **11**, 1513 (1980).

[19] H. R. Child and J. W. Cable, Phys. Rev. B **13**, 227 (1976).

[20] P. Radhakrishna and F. Livet, Solid State Commun. **25**, 597 (1978).

[21] F. Kajzar and G. Parette, Phys. Rev. B **22**, 5471 (1980).

[22] N. I. Kulikov and C. Demangeat, Phys. Rev. B **55**, 3533 (1997).

[23] N. I. Medvedeva, D. C. V. Aken, and J. E. Medvedeva, J. Phys.: Condens. Matter **23**, 326003 (2011).

[24] H. Nakashima, Tetsu-to-Hagané **90**, 73 (2004).

[25] M. Yamaguchi, Metall. Mater. Trans. A **42**, 319 (2011).

[26] M. Yuasa and M. Mabuchi, Phys. Rev. B **82**, 094108 (2010).

[27] Y. Motohiro and M. Mamoru, J. Phys.: Condens. Matter **22**, 505705 (2010).

[28] G. Kresse and J. Furthmüller, Phys. Rev. B **54**, 11169 (1996).

[29] G. Kresse and D. Joubert, Phys. Rev. B **59**, 1758 (1999).

[30] J. P. Perdew, K. Burke, and M. Ernzerhof, Phys. Rev. Lett. **77**, 3865 (1996).

[31] H. J. Monkhorst and J. D. Pack, Phys. Rev. B **13**, 5188 (1976).

[32] M. Methfessel and A. T. Paxton, Phys. Rev. B **40**, 3616 (1989).

[33] See Supplemental Material at http://link.aps.org/supplemental/10.1103/PhysRevMaterials.3.013609 for the calculation results of other sites.

[34] L. Zhong, R. Wu, A. J. Freeman, and G. B. Olson, Phys. Rev. B **55**, 11133 (1997).

[35] E. Wachowicz and A. Kiejna, Comput. Mater. Sci. **43**, 736 (2008).

[36] J. S. Braithwaite and P. Rez, Acta Mater. **53**, 2715 (2005).

[37] C. S. Wang, B. M. Klein, and H. Krakauer, Phys. Rev. Lett. **54**, 1852 (1985).

[38] T. Asada and K. Terakura, Phys. Rev. B **46**, 13599 (1992).

[39] A. V. Ruban and I. A. Abrikosov, Rep. Prog. Phys. **71**, 046501 (2008).

[40] S. Suzuki, M. Obata, K. Abiko, and H. Kimura, Scr. Metall. **17**, 1325 (1983).

[41] S. Suzuki, S. Tanii, K. Abiko, and H. Kimura, Metall. Trans. A **18**, 1109 (1991).

[42] S. Suzuki, M. Obata, K. Abiko, and H. Kimura, Trans. Iron Steel Inst. Jpn. **25**, 62 (1985).